Optical signatures of Dirac nodal lines in $NbAs_2$

Yinming Shao[a,b,1], Zhiyuan Sun[a,b], Ying Wang[c], Chenchao Xu[d], Raman Sankar[e,f], Alexander J. Breindel[b], Chao Cao[g], Michael M. Fogler[b], Andrew J. Millis[a,h], Fangcheng Chou[e], Zhiqiang Li[i], Thomas Timusk[j,k], M. Brian Maple[b], and D. N. Basov[a,b]

[a]Department of Physics, Columbia University, New York, NY 10027; [b]Department of Physics, University of California at San Diego, La Jolla, CA 92093; [c]National High Magnetic Field Laboratory, Tallahassee, FL 32310; [d]Department of Physics, Zhejiang University, Hangzhou 310036, China; [e]Center for Condensed Matter Sciences, National Taiwan University, Taipei 10617, Taiwan; [f]Institute of Physics, Academia Sinica, Taipei 10617, Taiwan; [g]Department of Physics, Hangzhou Normal University, Hangzhou 310036, China; [h]Center for Computational Quantum Physics, Flatiron Institute, New York, NY 10010; [i]College of Physical Science and Technology, Sichuan University, Chengdu, Sichuan 610064, China; [j]Department of Physics and Astronomy, McMaster University, Hamilton, ON L8S 4M1, Canada; and [k]Quantum Materials Program, Canadian Institute for Advanced Research, Toronto, ON M5G 1Z8, Canada

Edited by Laura H. Greene, Florida State University, Tallahassee, FL, and approved November 15, 2018 (received for review June 21, 2018)

Using polarized optical and magneto-optical spectroscopy, we have demonstrated universal aspects of electrodynamics associated with Dirac nodal lines that are found in several classes of unconventional intermetallic compounds. We investigated anisotropic electrodynamics of $NbAs_2$ where the spin-orbit coupling (SOC) triggers energy gaps along the nodal lines. These gaps manifest as sharp steps in the optical conductivity spectra $\sigma_1(\omega)$. This behavior is followed by the linear power-law scaling of $\sigma_1(\omega)$ at higher frequencies, consistent with our theoretical analysis for dispersive Dirac nodal lines. Magneto-optics data affirm the dominant role of nodal lines in the electrodynamics of $NbAs_2$.

nodal-line semimetal | optical conductivity | magneto-optics | Dirac fermions

Nodal-line semimetals (NLSMs) are newly discovered quantum materials with linear bands and symmetry-protected band degeneracies. Compared with 3D Dirac/Weyl semimetals (Fig. 1*A*), the band touching in NLSMs (Fig. 1 *B* and *C*) is not constrained to discrete points but extends along lines in the Brillouin zone (BZ) (1–4). This unconventional band structure has been predicted to give rise to topologically nontrivial electronic phases (3). For example, the first Weyl semimetal phase discovered in the NbAs family (5–7) is ultimately rooted in nodal lines (8, 9). Despite intense theoretical interest (10–13) and numerous material predictions (3, 4), experimental results for NLSMs are sparse, with ZrSiS (14, 15) and $PbTaSe_2$ (16) being the only examples. The dominant tool in the search for topological nodal systems is angle-resolved photoemission spectroscopy (ARPES). In addition to ARPES, nontrivial topologies in quantum materials are often revealed via nontrivial response functions (4). Optical and magneto-optical probes are particularly well suited for investigating nontrivial bulk response functions (17, 18), subtle surface states (19), and Berry curvature effects [through nonlinear optics (4, 20)]. The nontrivial response functions in general NLSMs registered through power-law analysis are the subject of this study.

Power-law behavior of the real part of the optical conductivity ($\sigma(\omega)=\sigma_1(\omega)+i\sigma_2(\omega)$) over extended frequency [i.e., $\sigma_1(\omega)\sim\omega^{d-2}$ (21–23)] is a hallmark of Dirac-like nodal points in solids. Linear ($\sigma_1(\omega)\sim\omega$) and constant optical conductivity has been confirmed in 3D [e.g., pyrochlore iridates (24), Dirac semimetal Cd_3As_2 (25), and $ZrTe_5$ (26)] and 2D [e.g., graphene (27)], respectively. Note that the linear power-law conductivity may not extrapolate to zero (25) due to, for exampe, overlapping intraband contributions (28). Nevertheless, the constant (positive) slope of conductivity ($d\sigma_1/d\omega=const.$) is still anticipated. Here, we show experimentally and theoretically that energy-dispersive Dirac nodal lines can also give rise to linear optical conductivity. Similar to other Dirac materials (25, 27), the power law of $\sigma_1(\omega)$ may be terminated at the lowest frequencies by the opening of the low-lying gap 2Δ in Dirac band dispersion. However, at $\omega > 2\Delta$, the linear dispersion persists and inevitably gives rise to the attendant power law of $\sigma_1(\omega)$. In this regard, we refer to gapped nodal lines simply as nodal lines, and the node is understood as the "Dirac point" of the massive Dirac band (17, 29).

We explore the electrodynamics of nodal lines using $NbAs_2$ as a case study. The observed power-law behaviors in $\sigma_1(\omega)$ spectra are corroborated by density functional theory (DFT) calculations. Furthermore, the Dirac linear dispersion perpendicular to the lines has been identified via the square-root scaling of Landau levels (LLs) in magneto-optics, a fingerprint of systems with nodal points in the electronic structure (30–32). The notion of nodal lines established here through unusual response functions might also explain the exotic magnetoresistance properties of $NbAs_2$ (33–35).

Characteristic infrared responses of nodal intermetallic systems and their relationship to the electronic structure of Dirac/Weyl semimetals are displayed in Fig. 1. While the optical responses of the Weyl semimetal (Fig. 1*A*) and flat NLSM (Fig. 1*B*) have been studied extensively (17, 23–26, 28, 36), the response of the dispersive nodal line (Fig. 1*C*) remains underexplored (18). The optical conductivity spectrum of the dispersive nodal line (Fig. 1*C*) resembles that of Weyl cones at low energy, where $\sigma_1(\omega)\sim\omega$ or equivalently $d\sigma_1/d\omega=const.$ Above certain photon energy when the entire dispersive region is being interrogated by infrared photons, the conductivity power law approaches that of the flat nodal line. This characteristic behavior of $\sigma_1(\omega)$ outlines a straightforward approach in the search

Significance

The 3D nodal points in Dirac and/or Weyl semimetals are in the vanguard of quantum materials research. A hallmark of these systems is the linear band dispersion. This latter electronic stricture gives rise to unconventional transport and optical phenomena. Here, we demonstrate that solids with dispersive nodal lines in the electronic structure share many common aspects with the response of 3D nodal-points systems. We investigated $NbAs_2$ using a combination of optical and magneto-optical techniques and have identified electromagnetic signature of dispersive nodal lines. This particular compound has allowed us to inquire the impact of spin-orbit coupling on the universal characteristic of nodal metals.

Author contributions: Y.S. and D.N.B. designed research; Y.S., Z.S., Y.W., C.X., R.S., and A.J.B. performed research; Y.S., Z.S., Y.W., and D.N.B. analyzed data; and Y.S., Z.S., Y.W., C.X., R.S., A.J.B., C.C., M.M.F., A.J.M., F.C., Z.L., T.T., M.B.M., and D.N.B. wrote the paper.

The authors declare no conflict of interest.

This article is a PNAS Direct Submission.

See Commentary on page 1084.

[1]To whom correspondence should be addressed. Email: ys2956@columbia.edu.

This article contains supporting information online at www.pnas.org/lookup/suppl/doi:10.1073/pnas.1809631115/-/DCSupplemental.

Published online December 17, 2018.

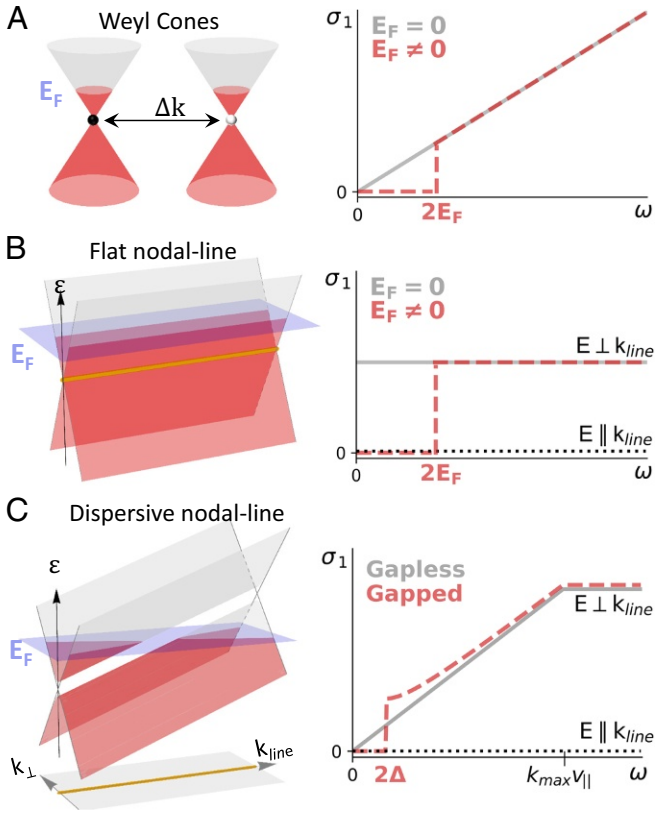

Fig. 1. Band structure schematic (*Left*) and corresponding optical conductivity (*Right*) for 3D Weyl cones (*A*), flat nodal line (*B*), and dispersive nodal line (*C*). Red color in the band structure schematic indicates filled electronic states. Gray lines and dashed red lines in the optical conductivity represent gapless and gapped responses, respectively. In *A* and *B*, the optical gap comes from finite doping ($E_F \neq 0$), while the electronic structure is gapless. Note that the conductivity spectra in *A* apply to Dirac nodes as well. For *C*, the gap originates from SOC, and the bands are dispersive along the line direction k_{line}. The orange line in *C* is the nodal line projected in momentum space.

and investigation of the NLSM physics. We stress that in realistic materials, the energy dispersion of the nodal structure, finite offsets of the Fermi energy ($E_F \neq 0$), and/or energy gaps derived from spin-orbit coupling (SOC) lead to deviations from previous predictions that ignored these factors (36, 37).

A dispersive nodal line is described by the Dirac-like Hamiltonian (*SI Appendix*, section 2) with the band dispersion

$$\varepsilon_\pm = \pm\sqrt{\Delta^2 + v_1^2 k_1^2 + v_2^2 k_2^2} + v_\parallel k_\parallel, \qquad [1]$$

where $k_\parallel$ is the momentum along the nodal line, while k_1 and k_2 are those perpendicular to the nodal line. As schematically shown in Fig. 1*C*, there is a gradual energy shift along the k_{line} with slope quantified by the "velocity" $v_\parallel$. Perpendicular to the nodal line, the dispersion is Dirac-like with the asymptotic velocities v_1 and v_2. SOC induces a finite mass Δ. We have derived an analytical form for the real part of the optical conductivity of a generic nodal-line conductor with or without SOC (*SI Appendix*, section 2):

$$\sigma^i_{NL}(\omega) = \frac{N}{16}\frac{e^2}{h}k_0(\omega)\frac{v_i^2}{v_1 v_2}\left(1+\frac{4\Delta^2}{\omega^2}\right)\Theta(\omega - 2\Delta_{op}), \qquad [2]$$

where v_i is the asymptotic velocity along the electric field direction. Note that along the nodal-line direction, $v_3 = 0$ and the corresponding σ^3_{NL} vanishes. N is the degeneracy of nodal lines, e is electron charge, h is Planck's constant, $k_0(\omega)$ is the effective nodal-line length in **k**-space where optical transition actually takes place, Θ is the step function, 2Δ is the gap introduced by SOC, and $2\Delta_{op}$ is the optical gap ($2\Delta + 2E_F$). If the nodal-line length is independent of frequency [$k_0(\omega) = k_0$], the simple flat optical conductivity $\sigma_{NL}(\omega) \sim \frac{e^2}{h}k_0$ occurs above the gap. However, once frequency-dependent nodal-line length is considered, the optical conductivity attains the same frequency dependence as $k_0(\omega)$. Therefore, $\sigma_{NL}(\omega)$ provides direct access to the complex geometry of a nodal line in **k**-space via its length $k_0(\omega)$. For linearly dispersive nodal lines as described by Eq. **1**, we find that $k_0(\omega) = \omega/v_\parallel$ and the interband optical conductivity scales as $\sigma_1(\omega) \sim (v_i^2/v_1 v_2)\omega$. We remark that since $v_3 = 0$ along the nodal line, this $\sigma_1(\omega)$ resembles the optical conductivity of strongly anisotropic 3D Dirac points (see *SI Appendix*, section 2*C* for more discussion).

We display in Fig. 2 the results of the ab initio calculations of the nodal lines (orange) in $NbAs_2$ obtained by using DFT. Notably, the nodal lines in $NbAs_2$ are open-ended and extend indefinitely through multiple BZs. The directionality of the open nodal lines implies huge optical anisotropy since the dissipative part of the conductivity $\sigma_1(\omega)$ is predicted (18, 36, 37) to vanish along the nodal-line direction (Fig. 1 *B* and *C*). We remark that nodal lines are usually not fixed along high symmetry lines and therefore can elude only a cursory band structure inquiry. To avoid this potential shortcoming, we have performed 3D band structure calculations for $NbAs_2$ near *Y*-X_1 and I_1-*Z* (see Fig. 2*B* and see Fig. 4 *C* and *D*) in our search for the nodal-line dispersion in this compound (see also *SI Appendix*, Movies S1 and S2). The blue shaded area indicates the dispersive nodal-line region that dominates the

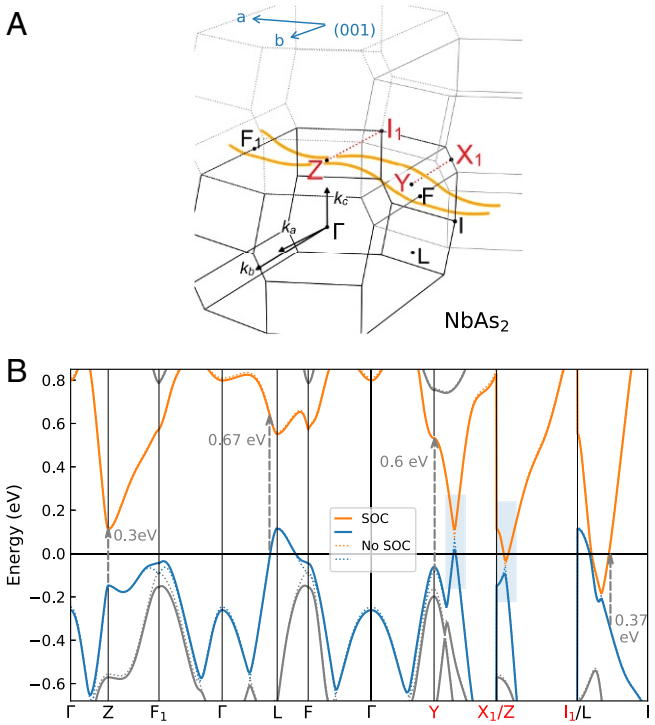

Fig. 2. (*A*) Ab initio calculations of the nodal lines (orange) in momentum space of $NbAs_2$. Red symbols are the high symmetry points in the BZ near the nodal lines. Blue arrows label the crystallographic axes in the (001) plane. (*B*) Band structure for $NbAs_2$ calculated along high symmetry points in *A*, with (solid lines) and without (dotted lines) SOC. Gray arrows indicate possible optical transitions.

low-energy (<0.3 eV) electrodynamics of $NbAs_2$ that we will analyze next.

The polarized reflectance spectra obtained for the (001) surface of $NbAs_2$ at 10 K are displayed in Fig. 3*A*. The *a*-axis reflectance (R^a) shows a pronounced plasma minimum (~125 meV) near the screened plasma frequency. In the *b*-axis data (R^b), the plasma edge appears broadened, and a sharp dip develops ~110 meV. Fig. 3*A* also reveals strong anisotropy in midinfrared energy arrange >50 meV.

In Fig. 3 *B*, *Left*, we display the 10 K optical conductivity for both polarizations of incident light. The Drude conductivity in both σ_1^a and σ_1^b feature multiple free-carrier components (*SI Appendix*, section 2D), consistent with multiple Fermi pockets revealed by quantum oscillation measurements (33–35). The most striking feature is the sharp double step in σ_1^b (green arrows), followed by $\sigma_1(\omega)\sim\omega$ relation over an extended frequency range. A somewhat weaker step structure and linear conductivity are also evident in σ_1^a. Interestingly, the double-step structure followed by a linear conductivity at higher frequencies resembles the response predicted for Weyl semimetals with inversion symmetry breaking (23). In this toy model with energy-shifted Weyl cones (23), Pauli blocking (forbidden optical transitions when the final states are filled) happens at different energies; hence, the predicted double step appears. Although no Weyl points exist in $NbAs_2$, the nodal lines give rise to linearly growing $\sigma_1(\omega)$ above the gaps, which we will focus on next.

Optical conductivities calculated using DFT are shown in Fig. 3 *B*, *Right*. The DFT spectra capture the gross features of the data, including the steps, the linear dependence, and the slope change at $E_{max}\sim0.3$ eV in both σ_1^a and σ_1^b. The anisotropy between σ_1^a and σ_1^b is also evident in the calculations. Importantly, while the linear slope extrapolates close to 0 at zero energy for σ_1^a, both the experiment and the calculations show a large, nonzero intercept for σ_1^b. This large intercept at zero energy is inconsistent with the optical conductivity model for 3D Dirac/Weyl fermions mentioned above (Fig. 1*A*). Instead, we show that the linear conductivity and the intercept result from the nodal line in $NbAs_2$. SOC triggers energy gaps along the nodal line (Fig. 4*E*), and the gap size changes from ~100 meV ($2\Delta_2$) near the high-symmetry line X_1-*Y* to ~80 meV ($2\Delta_1$) near I_1-*Z*. Both the X_1-*Y* direction and I_1-*Z* direction are parallel to the k_b direction (Fig. 4 and *SI Appendix*, Fig. S2). We demonstrate below that, while a flat nodal line (near X_1-*Y*) gives rise to constant $\sigma_1(\omega)$ (Fig. 1*B*), the dispersive nodal line near I_1-*Z* leads to linear conductivity (Fig. 1*C*) in $NbAs_2$. The combination of dispersive and flat nodal lines causes the linear optical conductivity with a large intercept observed both in experiment and in DFT calculation.

In Fig. 4*A*, we show $\sigma_1^b(\omega)$ data at three different temperatures. A notable feature of these data is the broadening of the step-like structure at higher temperatures. The blue dotted line is the fit to σ_1^b (10 K) using Eq. **2** and band structure parameters (*SI Appendix*, section 2D), showing excellent agreement with experiment. Gray dashed and solid lines display the contributions to the fit associated with interband transitions from the dispersive and flat nodal line, respectively. The fitting parameters are listed in *SI Appendix*, Table S1. With additional parameters (the angle between the nodal line and the *a* axis) from the band structure, we obtain fitted σ_1^a curves that are in excellent agreement with the experiment as well (*SI Appendix*, section 2D and Fig. S3). In Fig. 4 *B*–*D*, we plot the calculated band structure near I_1-*Z* and near X_1-*Y* for momentum directions k_{line} and k_b ($k_{line}\perp k_b$). The gray planes indicate constant Fermi energy (E_F). The side panels of Fig. 4*D* show the projected band structure along each direction, highlighting the extreme anisotropy of nodal lines. Fig. 4 *C* and *D* show two different segments of the same nodal line featuring near-linearly dispersing (near I_1-*Z*) and flat (near X_1-*Y*) regions. Note in Fig. 4*C* that there is a small tilt of the Dirac bands (38) that is not included in our nodal-line model, Eq. **1**.

An intuitive picture for the linear law of the optical conductivity from extended Pauli blocking is presented in Fig. 4*E*. Orange and blue dotted lines in Fig. 4*E* indicate the calculated gap energies at different line lengths k_0 (from I_1-*Z* to X_1-*Y*). Schematics of the Dirac cones are overlaid on the calculation to illustrate the band-filling level change along the line. Green vertical arrows indicate the onset of interband transition controlled by Pauli blocking. With increasing photon energy ($\omega_2>\omega_1$), longer segments of the nodal line ($k_0(\omega_2)>k_0(\omega_1)$) are being activated as Pauli blocking expands over growing phase space. The resulting $\sigma_1(\omega)$ grows linearly until the entire dispersive nodal line (k_{max}) is activated ($E_{max}\sim k_{max}v_{\|}$). For a gapless nodal line, the linear power law of $\sigma_1(\omega)$ extrapolates to zero at $\omega\to0$ (Fig. 1*C*). This simple picture of the dispersive nodal line captures the gross features of the conductivity data.

While the step in σ_1 is pinned to $2\Delta_1$ for the dispersive nodal-line crossing E_F (Figs. 1*C* and 4*C*), the step associated with the energy-flat nodal line occurs at $2\Delta_2 + 2E_{F2}$ (Figs. 1*B* and 4*D*). The constant optical conductivity causing the finite intercept is prominent in σ_1^b data and is nearly absent in σ_1^a. The

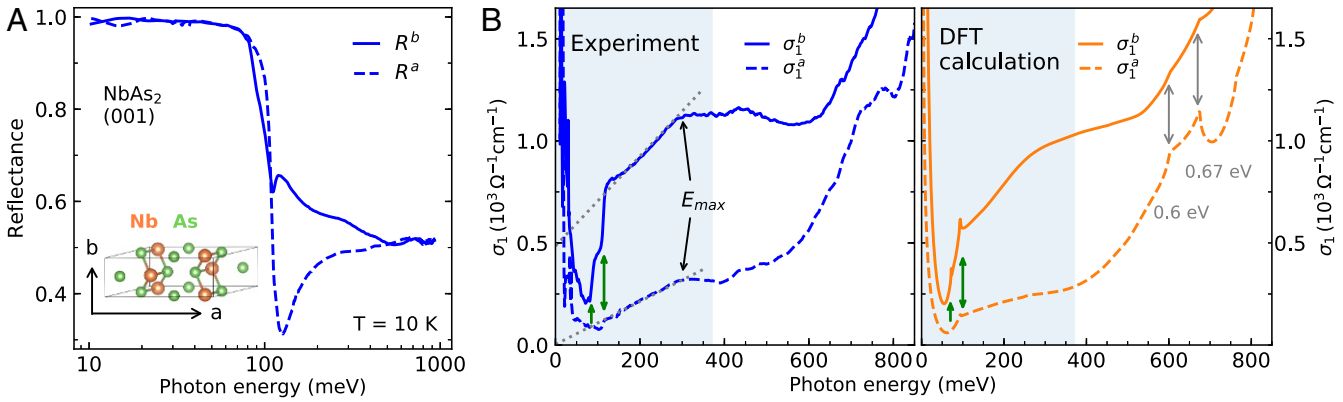

Fig. 3. (*A*) Anisotropic reflectance for the $NbAs_2$ (001) surface. *A*, *Inset* is a schematic of a unit cell of $NbAs_2$. (*B*) Optical conductivity from experiment (*Left*) and DFT calculations (*Right*). Blue shaded regions highlight the low-energy part where the response is dominated by the massive Dirac bands. Green arrows indicate positions of steps in $\sigma_1(\omega)$. Solid and dashed lines indicate the *b*-axis and *a*-axis response, respectively.

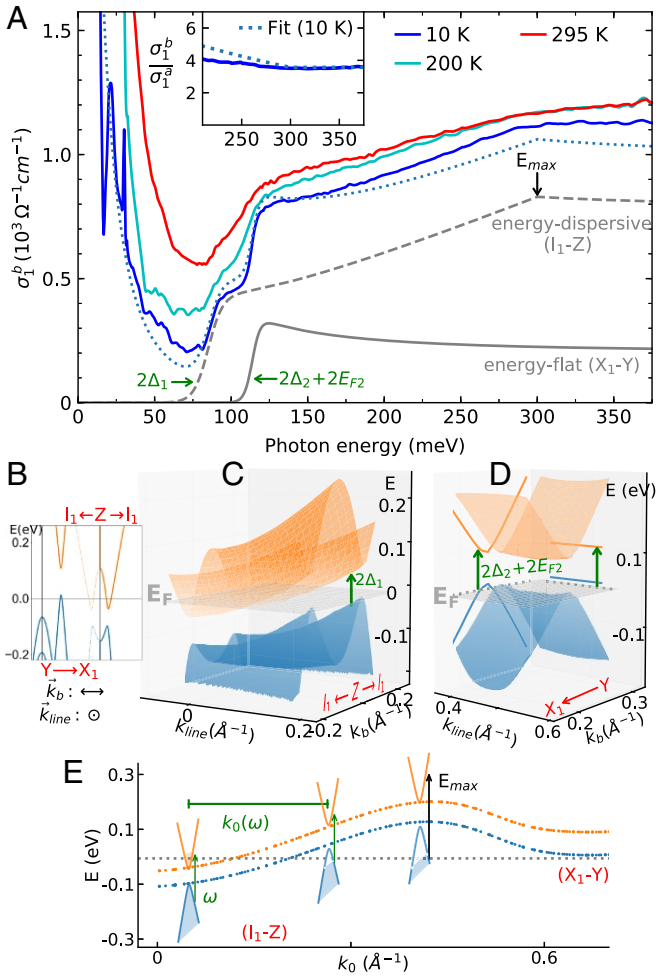

Fig. 4. (*A*) Optical conductivity for E || *b*. Blue dotted lines are fitted σ_1^b curves with nodal-line structure parameters. Gray dashed and solid lines denote contributions from the nodal lines near I_1-Z (*C*) and near X_1-Y (*D*), respectively. The linear increase of $\sigma_1^b(\omega)$ saturates at E_{max}~0.3 eV. *A*, *Inset* shows the ratio σ_1^b/σ_1^a above the gap region. *B* displays the results of band structure calculations along high-symmetry points near the nodal-line regions. The 3D version of the band structure calculation is shown in *C* and *D*. Green arrows illustrate onsets of interband transitions for dispersive (*C*) and energy-flat (*D*) segments of the nodal line. (*E*) The energy dispersion of the gapped nodal line displayed as a function of the line length k_0, calculated by using DFT. Dirac-cone schematics indicate different fillings of the Dirac bands along the line. The gray dotted line is the Fermi energy E_F. Vertical arrows show different onsets of interband transition, and horizontal arrows are the effective line length.

latter behavior is not surprising since the nodal line is nearly parallel to the a axis (*SI Appendix*, section 2D). According to Eq. **2**, the anisotropy of the conductivity should also be frequency-independent above the gap energy $[\sigma_1^b/\sigma_1^a \sim (v_b/v_a)^2]$, in agreement with the experiment (Fig. 4 *A*, *Inset*). The anisotropy of optical conductivities is therefore consistent not only with the existence of both flat and dispersive nodal lines in $NbAs_2$, but also with the suppression of conductivity along the nodal line. We emphasize that the large optical anisotropy is directly associated with open-ended nodal lines in $NbAs_2$, and the flat σ_1^b/σ_1^a spectral response (Fig. 4 *A*, *Inset*) is distinct from other anisotropic systems (39, 40).

Having established the zero-field signatures of nodal-line fermions, we set out to explore the properties of these anisotropic Dirac quasiparticles through magneto-optics. The electromagnetic signature of massive Dirac systems is the LLs dispersing from the gap energy 2Δ (26), which go through a linear to $\sqrt{B}$ cross-over with increasing B-field. In contrast, parabolic bands yield a scaling of LLs that is linear in B (31). These two distinct trends allow one to identify the Dirac dispersion perpendicular to the nodal lines. Unpolarized light was used for magneto-reflectance measurement up to 17.5 T at the National High Magnetic Field Laboratory (Fig. 5*A*). A series of peaks (labeled 0–3) hardened with increasing B field, and a weaker feature was evident at lower energy (~85 meV).

Noticing a remarkable similarity of the higher step energy in Fig. 4*A* (~120 meV) and peak energies in Fig. 5*A* (>120 meV at 3 T), we attributed the peaks in $R(B)/R(0\ T)$ to the interband LL transitions across the gapped Dirac bands. We also performed polarized magneto-reflectance measurements using an in-house 8-T apparatus (Fig. 5 *B* and *C*), enabling better signal-to-noise at low magnetic fields (41) (*SI Appendix*, Fig. S7). In Fig. 5*B*, we plot the derivative contour dR/dB, which emphasizes the peaks in $R(B)/R(0\ T)$ as a zero derivative (white) region bounded by positive (red) and negative (blue) derivative. The derivative plot is extremely sensitive to weak features in $R(B)/R(0\ T)$ and has been successfully used to investigate the subtle but important features in topological insulator surface states (19).

We obtained dR/dB contours for both $E \parallel b$ and $E \parallel a$ polarizations, and they showed similar features associated with peaks above the gap $2\Delta_2$. The features related to the smaller gap $2\Delta_1$ were only present for $E \parallel b$, but were completely suppressed for $E \parallel a$. Interestingly, while σ_1^a was smaller than σ_1^b (Fig. 3*B*), the amplitude of the $R(B)/R(0\ T)$ was larger for $E \parallel a$ than for $E \parallel b$ (*SI Appendix*, Fig. S7). Furthermore, the dR/dB plot for $E \parallel b$ polarization (Fig. 5*B*) shows prominent structure (gray dashed lines) intercepting the frequency axis at ~95 meV, in between the two gap energies ($2\Delta_1$ and $2\Delta_2$). This finite intercept at $B \to 0$ T is anomalous, and the exact nature of these resonances is a subject of future studies. An intriguing possibility pertains to the predicted topological surface states (42–44), with anisotropic behavior from DFT calculation (*SI Appendix*, Fig. S8).

Besides uncovering subtle magneto-optics features, the derivative plot dR/dB directly visualizes the $\sqrt{B}$ scaling of LL transitions in $NbAs_2$. For massive Dirac nodal lines, we have derived the following LL spectrum (*SI Appendix*, section 3):

$$E_{\pm n} = \pm\sqrt{2e\hbar|n|Bv_1v_2\cos(\phi) + \Delta^2}, \qquad [3]$$

where n is the LL index and ϕ is the angle between local nodal-line direction and magnetic field. Δ is the half-gap that characterizes the mass of the Dirac fermions (26) $m^D_{x,y,z} = \Delta/v^2_{x,y,z}$, and the $\pm$ selects the conduction/valence band LLs. The dipole selection rules (26, 30, 31) for interband LL transitions are $\delta|n| = |n|' - |n| = \pm 1$. The transition energy is therefore:

$$E_T = \sqrt{2e\hbar|n|B\overline{v}^2 + \Delta^2} + \sqrt{2e\hbar(|n|+1)B\overline{v}^2 + \Delta^2}, \qquad [4]$$

where the effective velocity $\overline{v} = \sqrt{v_1v_2\cos(\phi)}$.

In Fig. 5 *B* and *C*, green dashed lines are fitted interband LL transitions using Eq. **4** with $\overline{v}$=2.53 eV·Å and a gap $2\Delta_2$ = 114 meV. The effective velocity is very close to the theoretical estimate (2.3 eV·Å) obtained from the same asymptotic velocities v_1, v_2 we used to model $\sigma_1(\omega)$ (*SI Appendix*, sections 2D and 3). Green dots are peak energies extracted from Fig. 5*A*, showing excellent agreement for $\sqrt{B}$-spaced interband LL transition across $2\Delta_2$ in both unpolarized and polarized data. The nonlinearly spaced LLs can be easily identified at fixed B, as higher-order LLs are closer-spaced in energy, in stark contrast to the behavior of systems with parabolic bands. The Dirac mass (26) $m^D_{ab} = \Delta_2/v_a v_b = 0.068\ m_e$ is ~4 times smaller

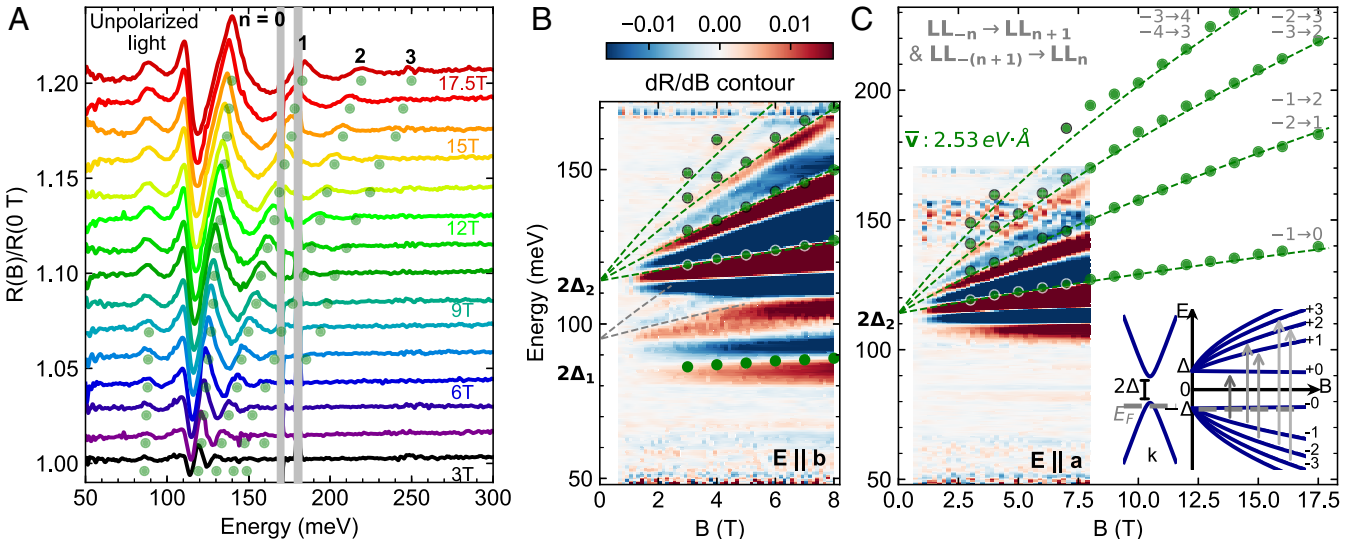

Fig. 5. (*A*) Magneto-reflectance spectra normalized by zero-field reflectance, showing a series of LL transitions systematically changing with increasing *B*. We also observe only a weakly field-dependent mode at ∼85 meV. (*B*) Derivative contour (*dR/dB*) for E || *b*. The energies of peaks extracted from *A* are displayed as green dots. Gray dashed lines indicate the subtle in-gap states. (*C*) *dR/dB* for E || *a* and peak energies extracted from *A*. Green dashed lines in *B* and *C* are fits using Eq. **4** with $\bar{v} \sim 2.53\,eV \cdot \AA$ and $2\Delta_2 = 114$ meV. *C*, *Inset* shows gapped Dirac bands and the LL dispersion with magnetic field *B*. Arrows indicate allowed interband LL transitions across the gap.

compared with parabolic carriers (0.24–0.29 m_e) (33, 34). This much smaller mass implies that the high mobility carriers in $NbAs_2$ are likely to originate from massive Dirac fermions in the nodal lines.

The extracted gap energy ($2\Delta_2 \sim 114$ meV) from fitting the LL dispersion is very close to the higher step energy in the zero-field data ($2\Delta_2 + 2E_{F2} \sim 120$ meV), indicating that the gapped cones are only weakly doped ($E_F < 5$ meV). This low doping level in the massive nodal lines (near X_1-Y) most certainly gives rise to a huge magneto-infrared response (*SI Appendix*, Fig. S7), since it can be easily driven into the extreme quantum limit when only the 0th LL is occupied. In contrast, the heavy trivial bands with large carrier density remain in the classical regime at the highest attainable field (17.5 T) (33, 34).

We now discuss the implication of massive Dirac nodal lines for the unusual magneto-resistance (MR) properties of $NbAs_2$. Giant MR $\{[\rho(B) - \rho(0)]/\rho(0) > 10^5\,\%\}$ in nonmagnetic $NbAs_2$ has been observed (33–35, 45) and explained as a cooperation of perfect electron-hole compensation and high-mobility carriers. These two effects are expected to produce a $\sim B^2$ increase of MR. However, high-field MR measurements clearly deviate from the B^2 dependence starting at ∼10 T and linearly increase with B without saturation (34). Such a large ($> 10^5\,\%$), nonsaturating behavior displaying a cross-over from (nearly) quadratic to linear scaling calls for interpretations beyond electron-hole compensation. We believe that the lightly doped Dirac nodal lines established here are crucial to understand the unusual MR in $NbAs_2$, as we will elucidate below.

The quantum linear MR (46, 47) reads as $\rho_{xx} = N_i B/\pi n^2 e$, where N_i is the scattering center concentration and n is the carrier density. Both the minority massive Dirac fermions in the quantum limit and the majority carriers in the classical two-band model can give rise to large MR. However, a slight deviation from perfect electron-hole compensation, which exists in $NbAs_2$, will cause the $\sim B^2$ rise of MR to saturate at a field-independent value (48), contrary to experiment (34). The existence of massive Dirac fermions may account for these discrepancies. At high field where the classical MR saturates, the quantum linear MR from Dirac fermions overwhelms other contributions, and hence the scaling law changes from quadratic to linear (47).

In summary, we discovered dispersive Dirac nodal lines in $NbAs_2$ and derived expressions for anisotropic response functions for a general case of dispersive nodal lines. Our results not only shed light on the interpretation of the exotic MR in this family of materials, but also pave the way for identifying new NLSMs using optical/magneto-optical spectroscopy. $NbAs_2$ therefore constitutes a concrete platform to explore various predictions for nodal-line fermions, including large spin Hall effect (49) and Floquet Weyl points (50–52). We remark that the energy-dispersive nodal line is a common aspect of the electronic structure in many solid-state systems, including: transition metal dipnictides ($NbAs_2$), ZrSiS (17), and even intermetallic superconductor MgB_2 (T_c = 39 K) (53, 54). The nodal-line band structure therefore governs rich physical phenomena registered through the analysis of the optical conductivity, LL transitions, MR along with nontrivial superconducting properties. Therefore, our experimental inquiry into the dispersive nodal lines has implications for a wide range of phenomena that are in the vanguard of current quantum materials research.

Materials and Methods

Millimeter-sized single crystals of $NbAs_2$ were grown using a chemical vapor transport method. The as-grown $NbAs_2$ single crystals have a prismatic rod shape along the *b*-direction with shiny and well-defined facets. The single crystal X-ray diffraction on these crystals is shown in *SI Appendix*, Fig. S1. Temperature-dependent infrared reflectance measurements were done using a Fourier-transform infrared spectrometer with standard gold-overfilling technique. High-field (17.5 T) magneto-optical measurements were done in the National High Magnetic Field Laboratory. Polarized low-field magneto-optical measurements were performed using an in-house apparatus (8 T) enabling higher signal-to-noise. Band structure and optical conductivity calculations were carried out based on DFT with the Vienna Abinitio Simulation Package; see *SI Appendix*, section 5 for details.

ACKNOWLEDGMENTS. This work was supported by Army Research Office Grant W911nf-17-1-0543. D.N.B. is the Moore Foundation Investigator, EPIQS Initiative Grant GBMF4533. F.C. was supported by the Ministry of Science and Technology in Taiwan Grant 106-2119-M-002-035-MY3. A portion of this work was performed at the National High Magnetic Field Laboratory, which is supported by National Science Foundation Cooperative Agreement DMR-1157490 and the State of Florida. A.J.B. and M.B.M. were supported by US Department of Energy, Office of Basic Energy Sciences, Division of Materials Sciences and Engineering Grant DEFG02-04-ER46105.

1. Burkov AA, Hook MD, Balents L (2011) Topological nodal semimetals. *Phys Rev B* 84:235126.
2. Fang C, Chen Y, Kee HY, Fu L (2015) Topological nodal line semimetals with and without spin-orbital coupling. *Phys Rev B* 92:081201.
3. Weng H, Dai X, Fang Z (2016) Topological semimetals predicted from first-principles calculations. *J Phys Condens Matter* 28:303001.
4. Armitage NP, Mele EJ, Vishwanath A (2018) Weyl and Dirac semimetals in three-dimensional solids. *Rev Mod Phys* 90:015001.
5. Xu SY, et al. (2015) Discovery of a Weyl fermion state with Fermi arcs in niobium arsenide. *Nat Phys* 11:748–754.
6. Lv BQ, et al. (2015) Observation of Weyl nodes in TaAs. *Nat Phys* 11:724–727.
7. Xu SY, et al. (2015) Discovery of a Weyl fermion semimetal and topological Fermi arcs. *Science* 349:613–617.
8. Lee CC, et al. (2015) Fermi surface interconnectivity and topology in Weyl fermion semimetals TaAs, TaP, NbAs, and NbP. *Phys Rev B* 92:235104.
9. Huang SM, et al. (2015) A Weyl Fermion semimetal with surface Fermi arcs in the transition metal monopnictide TaAs class. *Nat Commun* 6:7373.
10. Liu J, Balents L (2017) Correlation effects and quantum oscillations in topological nodal-loop semimetals. *Phys Rev B* 95:075426.
11. Yan Z, Huang PW, Wang Z (2016) Collective modes in nodal line semimetals. *Phys Rev B* 93:085138.
12. Lim LK, Moessner R (2017) Pseudospin vortex ring with a nodal line in three dimensions. *Phys Rev Lett* 118:016401.
13. Nie S, Xu G, Prinz FB, Zhang SC (2017) Topological semimetal in honeycomb lattice LnSI. *Proc Natl Acad Sci USA* 114:10596–10600.
14. Schoop LM, et al. (2016) Dirac cone protected by non-symmorphic symmetry and three-dimensional Dirac line node in ZrSiS. *Nat Commun* 7:11696.
15. Neupane M, et al. (2016) Observation of topological nodal fermion semimetal phase in ZrSiS. *Phys Rev B* 93:201104.
16. Bian G, et al. (2016) Topological nodal-line fermions in spin-orbit metal $PbTaSe_2$. *Nat Commun* 7:10556.
17. Schilling MB, Schoop LM, Lotsch BV, Dressel M, Pronin AV (2017) Flat optical conductivity in ZrSiS due to two-dimensional Dirac bands. *Phys Rev Lett* 119:187401.
18. Ahn S, Mele EJ, Min H (2017) Electrodynamics on Fermi cyclides in nodal line semimetals. *Phys Rev Lett* 119:147402.
19. Schafgans AA, et al. (2012) Landau level spectroscopy of surface states in the topological insulator $Bi_{0.91}Sb_{0.09}$ via magneto-optics. *Phys Rev B* 85:195440.
20. Morimoto T, Nagaosa N (2016) Topological nature of nonlinear optical effects in solids. *Sci Adv* 2:e1501524.
21. Hosur P, Parameswaran SA, Vishwanath A (2012) Charge transport in Weyl semimetals. *Phys Rev Lett* 108:046602.
22. Bácsi Á, Virosztek A (2013) Low-frequency optical conductivity in graphene and in other scale-invariant two-band systems. *Phys Rev B* 87:125425.
23. Tabert CJ, Carbotte JP, Nicol EJ (2016) Optical and transport properties in three-dimensional Dirac and Weyl semimetals. *Phys Rev B* 93:085426.
24. Sushkov AB, et al. (2015) Optical evidence for a Weyl semimetal state in pyrochlore $Eu_2Ir_2O_7$. *Phys Rev B* 92:241108.
25. Neubauer D, et al. (2016) Interband optical conductivity of the [001]-oriented Dirac semimetal Cd_3As_2. *Phys Rev B* 93:121202.
26. Chen ZG, et al. (2017) Spectroscopic evidence for bulk-band inversion and three-dimensional massive Dirac fermions in ZrTe5. *Proc Natl Acad Sci USA* 114:816–821.
27. Li ZQ, et al. (2008) Dirac charge dynamics in graphene by infrared spectroscopy. *Nat Phys* 4:532–535.
28. Chen RY, et al. (2015) Optical spectroscopy study of the three-dimensional Dirac semimetal $ZrTe_5$. *Phys Rev B* 92:075107.
29. Patri AS, Hwang K, Lee HW, Kim YB (2018) Theory of large intrinsic spin Hall effect in iridate semimetals. *Sci Rep* 8:8052.
30. Orlita M, et al. (2011) Carrier scattering from dynamical magnetoconductivity in quasineutral epitaxial graphene. *Phys Rev Lett* 107:216603.
31. Shao Y, et al. (2017) Faraday rotation due to surface states in the topological insulator (Bi1–xSbx)2Te3. *Nano Lett* 17:980–984.
32. Shuvaev AM, et al. (2017) Band structure of a two-dimensional Dirac semimetal from cyclotron resonance. *Phys Rev B* 96:155434.
33. Shen B, Deng X, Kotliar G, Ni N (2016) Fermi surface topology and negative longitudinal magnetoresistance observed in the semimetal $NbAs_2$. *Phys Rev B* 93:195119.
34. Yuan Z, Lu H, Liu Y, Wang J, Jia S (2016) Large magnetoresistance in compensated semimetals $TaAs_2$ and $NbAs_2$. *Phys Rev B* 93:184405.
35. Li Y, et al. (2016) Negative magnetoresistance in topological semimetals of transition-metal dipnictides with nontrivial Z2 indices. arXiv:1603.04056.
36. Mukherjee SP, Carbotte JP (2017) Transport and optics at the node in a nodal loop semimetal. *Phys Rev B* 95:214203.
37. Carbotte JP (2017) Optical response of a line node semimetal. *J Phys Condens Matter* 29:045301.
38. Wang R, Go A, Millis A (2017) Weyl rings and enhanced susceptibilities in pyrochlore iridates: $k \cdot p$ analysis of cluster dynamical mean-field theory results. *Phys Rev B* 96:195158.
39. Nakajima M, et al. (2011) Unprecedented anisotropic metallic state in undoped iron arsenide BaFe2As2 revealed by optical spectroscopy. *Proc Natl Acad Sci USA* 108:12238–12242.
40. Frenzel AJ, et al. (2017) Anisotropic electrodynamics of type-II Weyl semimetal candidate WTe_2. *Phys Rev B* 95:245140.
41. LaForge AD, et al. (2010) Optical characterization of Bi_2Se_3 in a magnetic field: Infrared evidence for magnetoelectric coupling in a topological insulator material. *Phys Rev B* 81:125120.
42. Xu C, et al. (2016) Electronic structures of transition metal dipnictides XPn_2 (X = Ta, Nb; Pn = P, As, Sb). *Phys Rev B* 93:195106.
43. Gresch D, Wu Q, Winkler GW, Soluyanov AA (2017) Hidden Weyl points in centrosymmetric paramagnetic metals. *New J Phys* 19:035001.
44. Luo Y, et al. (2016) Anomalous electronic structure and magnetoresistance in TaAs2. *Sci Rep* 6:27294.
45. Wang YY, Yu QH, Guo PJ, Liu K, Xia TL (2016) Resistivity plateau and extremely large magnetoresistance in $NbAs_2$ and $TaAs_2$. *Phys Rev B* 94:041103.
46. Abrikosov AA (1998) Quantum magnetoresistance. *Phys Rev B* 58:2788–2794.
47. Huynh KK, Tanabe Y, Tanigaki K (2011) Both electron and hole Dirac cone states in $BaFeAs_2$ confirmed by magnetoresistance. *Phys Rev Lett* 106:217004.
48. Ali MN, et al. (2014) Large, non-saturating magnetoresistance in WTe_2. *Nature* 514:205–208.
49. Sun Y, Zhang Y, Liu CX, Felser C, Yan B (2017) Dirac nodal lines and induced spin Hall effect in metallic rutile oxides. *Phys Rev B* 95:235104.
50. Yan Z, Wang Z (2016) Tunable Weyl points in periodically driven nodal line semimetals. *Phys Rev Lett* 117:087402.
51. Narayan A (2016) Tunable point nodes from line-node semimetals via application of light. *Phys Rev B* 94:041409.
52. Chan CK, Oh YT, Han JH, Lee PA (2016) Type-II Weyl cone transitions in driven semimetals. *Phys Rev B* 94:121106.
53. Jin KH, et al. (2017) Topological Dirac-nodal-line semimetal phase in high-temperature superconductor MgB2. arXiv: 1710.06996.
54. Zhou X, et al. (2018) Observation of topological surface state in high temperature superconductor MgB2. arXiv: 1805.09240.